Additive Manufacturing 75 (2023) 103731

Contents lists available at ScienceDirect

Additive Manufacturing

journal homepage: www.elsevier.com/locate/addma

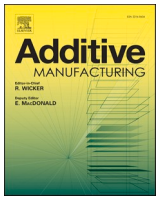

Functional bioglass/carbon nanocomposite scaffolds from vat photopolymerization of a novel preceramic polymer-based nanoemulsion

Franco M. Stabile [a,b], Alessia Famengo [c], Danilo Pedron [d], Hamada Elsayed [e,f], Enrico Bernardo [e,*]

[a] Technology Center of Mineral resources and Ceramic (CETMIC), CIC-CONICET-UNLP, Manuel B. Gonnet, B1897, Argentina
[b] Department of Chemical Engineering, Universidad Nacional de La Plata, B1900ADU, La Plata, Argentina
[c] National Research Council of Italy (CNR), Institute of Condensed Matter Chemistry and Technologies for Energy (ICMATE), 35127, Padova, Italy
[d] Department of Chemical Sciences (DiSC), University of Padova, 35131, Padova, Italy
[e] Department of Industrial Engineering, Università degli Studi di Padova, 35131, Padova, Italy
[f] Refractories, Ceramics and Building Materials Department, National Research Centre, Dokki, 12622 Cairo, Egypt

ARTICLE INFO

Keywords:
Preceramic polymers
Vat photopolymerization
Emulsions
Nanocomposites
Bioglass

ABSTRACT

Silicone polymers are already known as feedstock for a variety of silicate bioceramics, in the form of scaffolds with complex shapes, obtained by Vat Photopolymerization. Printing is enabled by using silicone blended with photocurable acrylates. The development of a particular silicate composition that functions as a glass or glass-ceramic precursor is possible by the addition of suitable oxide fillers (especially carbonate powders), suspended in the polymer blend. Oxides, from the fillers, easily react with silica left by the thermal transformation of the silicone. The fillers, however, also determine complications in Vat Photopolymerization, due to light scattering; in addition, local oxide concentrations generally impede the obtainment of glassy products. The present paper illustrates a simple solution to these issues, based on the inclusion of a Ca salt in nano-emulsion within a silicone-containing blend. Homogeneous printed samples are later converted into crack-free, fully amorphous ceramic composites, by firing at only 700 °C. The glass matrix, resembling 70S30C (70 % SiO_2 and 30 % CaO) bioglass, is achieved according to the quasi-molecular CaO distribution. The secondary phase, promoted by treatment in N_2 atmosphere and consisting of pyrolytic carbon, provides a marked photothermal effect.

1. Introduction

Processing routes based on the use of preceramic polymers have long been employed to produce advanced ceramic components that possess features and properties that cannot be achieved with traditional high-temperature solid state processing methods [1]. An advantage of the preceramic polymers processing is that conventional plastic shaping processes (such as fiber spinning, injection moulding, extrusion, additive manufacturing, etc.) can be applied, enabling the obtainment of ceramic products with complex shapes, which otherwise would be difficult to produce.

Silicones (polyorganosiloxanes) – having a generic $(RR'Si\text{-}O\text{-})_n$ molecular structure, where R and R' are side hydrocarbon chains –, are comprised among preceramic polymers, i.e. polymers undergoing conversion into ceramics upon heat treatment [1]. Thermal treatments above 500 °C trigger a polymer-to-ceramic transformation (ceramization), leading to a ceramic residue with a chemical composition in turn dependent on the firing atmosphere (e.g. silicon oxycarbide, SiOC, in N_2 or Ar, and silica, SiO_2, in O_2 or Air). According to the formulation, the ceramic yield (amount of ceramic residue for a certain mass of preceramic polymer) is quite variable. The residue deriving from high-yield silicones may be useful as a starting point for numerous ceramic systems, developed by addition of nano- and micro-sized inorganic reactive fillers [2,3]. Recent investigations have highlighted the feasibility of the addition alkaline and alkaline-earth metals oxides, carbonates, phosphates or even oxide glasses, giving rise to multiphase ceramics with microstructures similar to that of several glass-ceramic systems for application in bone tissue engineering, as shown by Dasan et al. and Elsayed et al. [4,5].

The latter investigations constitute a reference point concerning the application of vat photopolymerization technology, which is known as an additive manufacturing technology capable of generating complex

* Corresponding author.
E-mail address: enrico.bernardo@unipd.it (E. Bernardo).

https://doi.org/10.1016/j.addma.2023.103731
Received 12 April 2023; Received in revised form 25 June 2023; Accepted 7 August 2023
Available online 9 August 2023

shaped objects with high definition. The same investigations also concern the obtainment of photocurable materials. An easy way to obtain photocurable silicones is the incorporation of silicones into commercial photocurable resins, to produce engineered blends, without the need to adopt complex procedures for the acrylic functionalization of not-photocurable silicones or to use commercial photocurable silicones, which are expensive and exhibit a low ceramic yield [6,7]. In fact, silicones with high ceramic yield may be conveniently blended with acrylic photocurable resins, with or without added solvents. For instance, powdered commercial H44 resin can be directly dissolved in acrylates [4].

If incorporating reactive powder fillers, silicone-based photocurable blends are sensitive to typical drawbacks of suspensions adopted in vat photopolymerization 3D printing. Suspended particles, which have a marked difference in refraction index with respect to the liquid, produce an undesirable scattering effect leading to a poor printing resolution [8,9]. In addition, inorganic particles are difficult to disperse in organic medium, so sedimentation may occur. This could cause composition gradients in the printed structures. Both phenomena may be avoided if inorganic components sufficiently small (e.g. nanoparticles) are well dispersed [10,11]. In the present investigation, we rely on a different concept: vat photopolymerization is not supported by nanoparticles directly suspended in a photocurable liquid, but by a novel nano-emulsion.

Nanoemulsions are defined as dispersions of liquid nanometric droplets (dispersed phase) into another completely immiscible liquid (continuous phase). The dispersions are stabilized by the introduction of surface-active amphiphilic compounds (surfactants), and the droplet size is in the order of 50–200 nm [12]. Contrary to microemulsions, which may present different droplet sizes and complex structures, nanoemulsions are not stabilized thermodynamically but kinetically [13], and they can be produced by using a much lower surfactant concentration. Nanoemulsions have an optically transparent or translucent appearance [14].

Water-in-oil (W/O) and oil-in-water (O/W) emulsions can be distinguished based on the characteristics of the dispersed phase. The affinity of surfactant for the organic or the aqueous phase is determined by its hydrophilic-lipophilic balance (HLB). High HLB surfactants tend to stabilize O/W emulsion, while low HLB surfactants are used for W/O emulsions. Emulsions can be also stabilized using nanoparticles, which are absorbed at the liquid-liquid interphase (Pickering stabilization). Both pickering and surfactants can be used at the same time to obtain a synergic effect that produce more stable emulsions [15].

Span 20 and Span 80 (Sorbitan monooleate, HLB 8.6 and 4.3, respectively) are two examples of surfactants used to create W/O nanoemulsions [16] and hydrophobic silica nanoparticles are used for Pickering stabilization [17]. In addition, the incorporation of an electrolyte to the aqueous phase is known to improve the stability of the emulsion [18].

The present paper aims at presenting a synergistic approach to advanced 3D printing of polymer-derived ceramics. The concept of nano-emulsions is applied to the dispersion of a calcium salt in a photocurable silicone-containing blend, with the help of an adequate surfactant. The homogeneity in the dispersion is useful in the perspective of both printing resolution (due to reduced scattering, from small droplets) and phase evolution upon thermal transformation. In fact, the quasi molecular mixing of silica (from silicone and minor addition of fumed silica, added as stabilizer) and CaO (from the salt) led, after firing at 700 °C, to homogeneous and crack-free scaffolds. These scaffolds featured a glass matrix resembling 70S30C bioglass (70 mol% SiO_2, 30 mol% CaO), with the additional benefit of the inclusion of pyrolytic amorphous carbon, in turn promoting a photothermal effect.

2. Experimental procedure

2.1. Preparation and 3D printing of silicone-based emulsions

An 'oily' phase was prepared by dissolving 6.1 g of silicone resin (Silres H44, Wacker Chemie AG) in 20 g of a commercial photocurable resin (Standard Blend Transparent, FunToDo, Alkmaar, The Netherlands) under magnetic stirring for 30 min 2 g of Span 80 surfactant (Sorbitan Monooleate, TCI-Tokyo Chemical Industry) and 1 g hydrophobic fumed silica (FS, i.e. Silica treated with octamethylcyclotetrasiloxane, Aerosil R106, Evonik Germany) were subsequently added, under magnetic stirring for 30 min, followed by sonication for 15 min, by means of an ultrasonic tip (Bandelin Sonopuls HD 2070, Berlin, Germany).

Calcium nitrate tetrahydrate (CaNT, $Ca(NO_3)_2{\cdot}4H_2O$, Scharlab, Barcelona, Spain) was used directly as the 'aqueous' phase, since it underwent melting simply due to the heating produced by the ultrasonic tip. The adopted H44/CaNT weight proportion was 1/1.19 [wt%], in turn calculated to produce 30 CaO-70 SiO_2 (mol%) glass (see later).

An emulsion was produced by adding the salt to the oily phase and subjecting to ultrasonic tip for 15 min with the help of a magnetic stirrer. After sonication, the emulsion was fast cooled to room temperature.

Scaffolds with diamond lattice structure were obtained using a masked stereolithography printer (Prusa SL1S, Prague, Czech Republic, operating at $\lambda = 405$ nm) using an exposure time of 8 s and layer thickness of 50 μm. After printing, the scaffolds were detached from the printing platform (initially immersed in the emulsion and progressively moving upwards) and subsequently cleaned. The cleaning was performed first by blowing compressed air and then by immersion in isopropyl alcohol bath for 10 s. At last, the structures were hardened into a curing chamber (Prusa CW1, Prague, Czech Republic, operating at $\lambda = 405$ nm) for 15 min, for polymerizing the remained uncured resin.

2.2. Characterization of printed components and final scaffolds

Morphological features of the printed components, before and after the heat treatment, were investigated using an optical stereomicroscopy (Carl Zeiss™ AxioCams Microscopy Camera, USA), to determine the appearance and homogeneity of the internal struts. Microstructural observations of heat-treated scaffolds were made by scanning electron microscopy (SEM, Eindhoven, Netherlands).

Some fragments of cured struts were subjected to preliminary tests, to follow the pyrolysis process and the thermal decomposition of CaNT. Tests were performed in flowing N_2 (100 ml/min) up to 850 °C with a 5 °C/min heating rate, in a DSC-TG thermal analyser (TGA/DSC^{3+} STAR® System, Mettler Toledo, Columbus, OH).

The thermal conversion was realized in a tube furnace (Carbolyte Gero Ltd., Hope Valley, UK), in flowing N_2. Heating rates of thermal treatment were selected taking into account temperature mass losses and thermal effects seen on DSC-TG analysis. In this way, thermal cycle was 0.5 °C/min up to 500 °C and dwell of 2 h followed by another ramp of 1 °C/min up to 700 °C and dwell of 1 h.

Powdered samples, before and after heat treatment, were analyzed in a Bruker AXS D8 Advance (Karlsruhe, Germany) from $2\theta = 10–70°$, with a 0.05° step and 2 s per step, using Cu Kα radiation and Ni filter. Furthermore, Raman and Fourier-transform infrared analysis (Infrared Spectroscopy (FTIR) model 2000, PerkinElmer, USA) were performed on powders from fired scaffolds. A homemade micro-Raman device, consisting of a single 320 mm focal length image spectrograph (Triax-320, Horiba Jobin Yvon) outfitted with a holographic 1800 g/mm grating and a liquid-nitrogen-cooled CCD detector (Horiba Symphony II), was used to gather a Raman spectrum. A Spectra-Physics Ar+ laser (Stabilite 2017–06S) performing at 514.5 nm served as the excitation source. The stray-light level was reduced using a 514.5 nm long-pass edge filter.

The Raman spectrum was captured using the 50X objective of an optical microscope (Olympus BX 40), which was optically linked to the

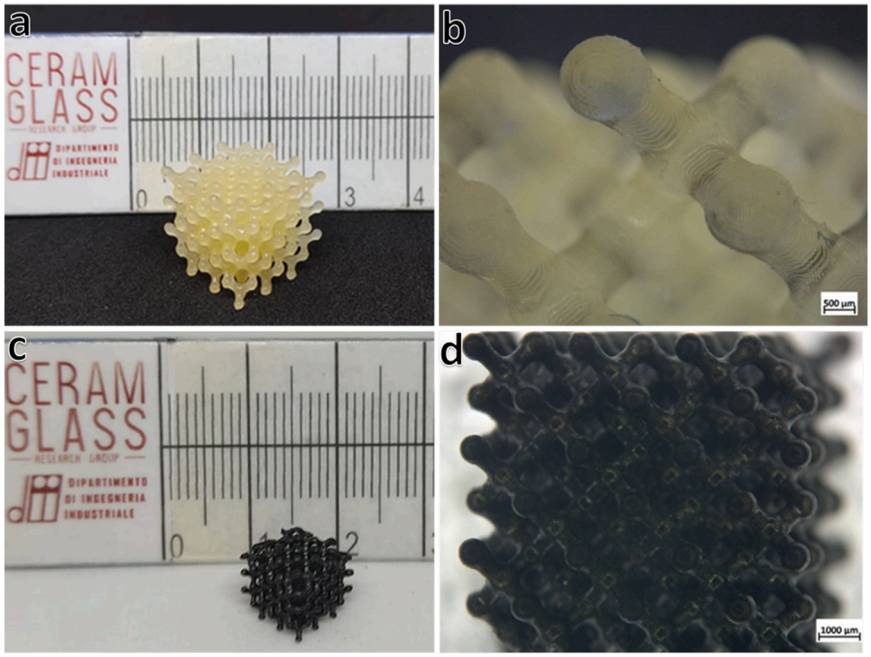

Fig. 1. (a,b) Detail of scaffold immediately after printing and UV curing; (c,d) scaffolds after firing at 700 °C in N_2 atmosphere.

spectrograph and had three objectives: 20X/0.35, 50X/0.75, and 100X/0.90 (Olympus SLMPL). The laser power on the sample was maintained below 0.8 mW to avoid heating and consequent possible damage to the material. The Bruker Advance III 300 spectrometer (Karlsruhe, Germany) was used for the NMR MAS testing. It features a 4 mm solid state probe, ZrO_2 rotors with Kel-F caps, and a magnetic field of 7.0 T, which matches the ^{29}Si and ^{13}C Larmor frequencies of 59.627 MHz and 75.46 MHz, respectively. The magic angle was precisely corrected before the data acquisition using KBr. The ^{29}Si single-pulse testing was recorded at a 6 kHz spinning frequency, 3000 transients, and a 60 s recycling delay. ^{29}Si chemical shift was externally referenced to solid (tetrakis) trimethylsylilsilane (Merck-Sigma-Aldrich, Darmstadt, Germany) at −9.84 ppm in relation to TMS. ^{13}C CP MAS experiment was measured at a spinning frequency of 11 kHz, with a variable amplitude cross-polarization ramp at a contact time of 1 ms, with 1H Spinal 64 decoupling, a recycling delay of 5 s and 5000 transients. Adamantane was used as an external standard.

The geometrical (bulk) density of heat-treated scaffolds was determined by measuring the mass and volume of the fired scaffold with an analytical balance and a digital caliper, respectively. While the He-gas pycnometer (Anton Paar Srl, Rivoli, Italy) was employed to measure the apparent density on entire samples (3D printed heat-treated scaffolds), and true density on pulverized samples obtained from printed parts. Then, the open, closed, and total porosities of the fabricated scaffolds were calculated based on the density values.

The compressive strength of scaffolds heat-treated at 700 °C was assessed using an universal testing machine (Galdabini Quasar 25, Italy), running with a 0.5 mm/min crosshead speed. The uniaxial compressive tests were conducted on samples of size 10 × 10 × 10 mm^3, perpendicular (⊥) to the building plane (i.e., z direction). Each data point represents the average value of at least 10 individual tests.

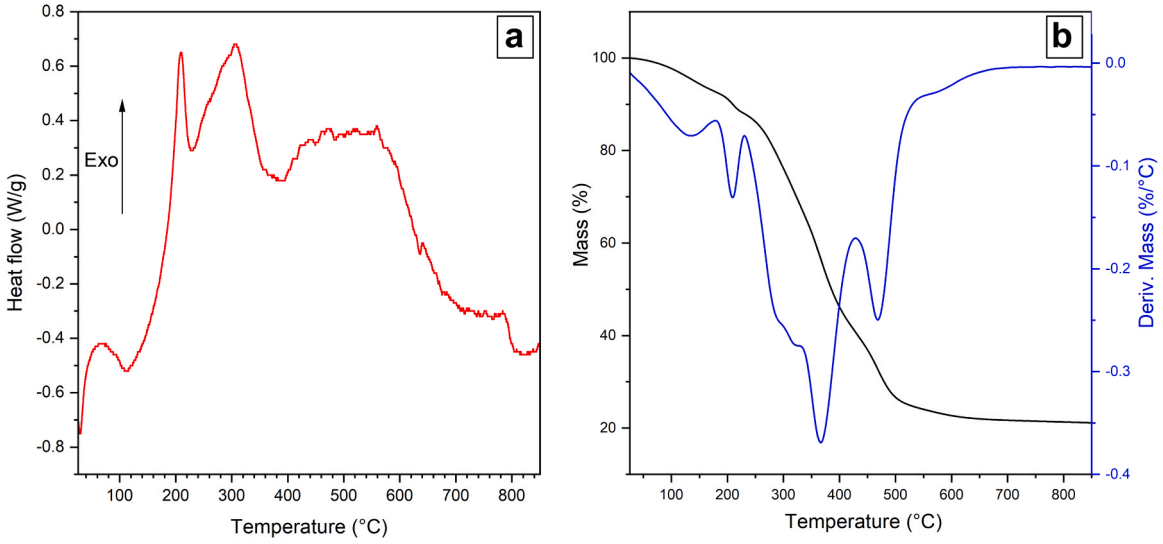

Fig. 2. Thermal evolution of printed silicone-based blend: (a) heat flow plot; (b) mass loss plots (experimental and derivative plots).

Table 1
Ceramic yield by component.

Component	Amount in batch (g)	Transformation	Expected yield (g)	Oxide yield (g)
Silres H44	6.1	Conversion into SiOC, yield of 0.72[4]	6.1 × 0.72 = 4.4	4.4 × 0.76 = 3.3 (SiO_2)
FS	1	Negligible loss	1	1 (SiO_2)
CaNT (~236 g/mol)	7.3	Decomposition into CaO (~56 g/mol)	7.3 × (56/236) = 1.7	1.7 (CaO)
Standard Blend Transparent + surfactant	22	Complete burn-out	0	-
Total	36.4		7.1 [7.1/36.4] = 19.5 %	6

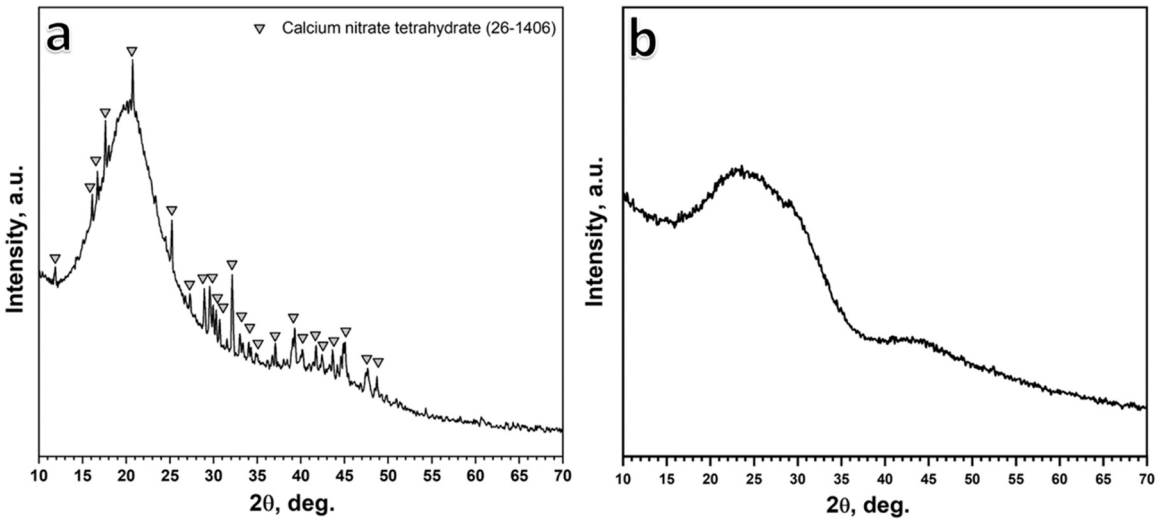

Fig. 3. X-ray diffraction analysis of silicone-based blend in the as-printed state (a) and after polymer to ceramic transformation; (b) at 700 °C.

3. Results and discussion

To overcome difficulties, in the printing phase, arising from coarsely dispersed particles, a first objective was the actual achievement of a nano-emulsion. This was assessed, at first, by observing the transparency of the liquid blend, before printing. The heating produced by sonication was reputed as sufficient to determine the melting of CaNT, in turn known for its low melting point (44 °C) [19]. The surfactant promoted the dispersion of liquid nano-sized droplets (forming a nano-emulsion), later turning in nanoparticles in the silicone-acrylic resin blend.

The printing was performed considering the recommended exposure time for the cross-linking of the adopted commercial photocurable material (2 s at λ = 405 nm, for 100 % acrylate resin). Operating with the silicone-containing mixture the exposure time was increased in proportion to the 'dilution' of acrylate resin operated by adding silicone, span 80 and salt to the photocurable resin (the acrylate resin corresponding to ≈60 wt%). The exposure time, in fact, was set to 8 s. Such assumption effectively led to sufficient hardening, forming scaffolds which could be easily detached from the printing platform, as shown by Fig. 1a. The homogeneity of printed components was confirmed by higher magnification optical stereomicroscopy (see Fig. 1b): the samples were nearly transparent, as an indication of the small droplet size of the

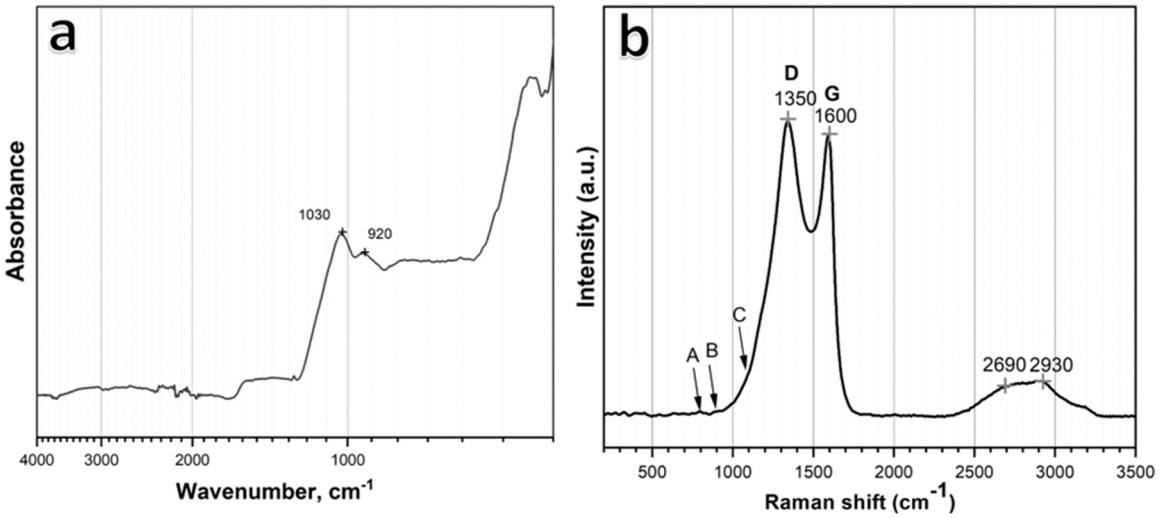

Fig. 4. (a) FTIR; (b) Raman spectra of the obtained bioglass-C composite (after firing at 700 °C).

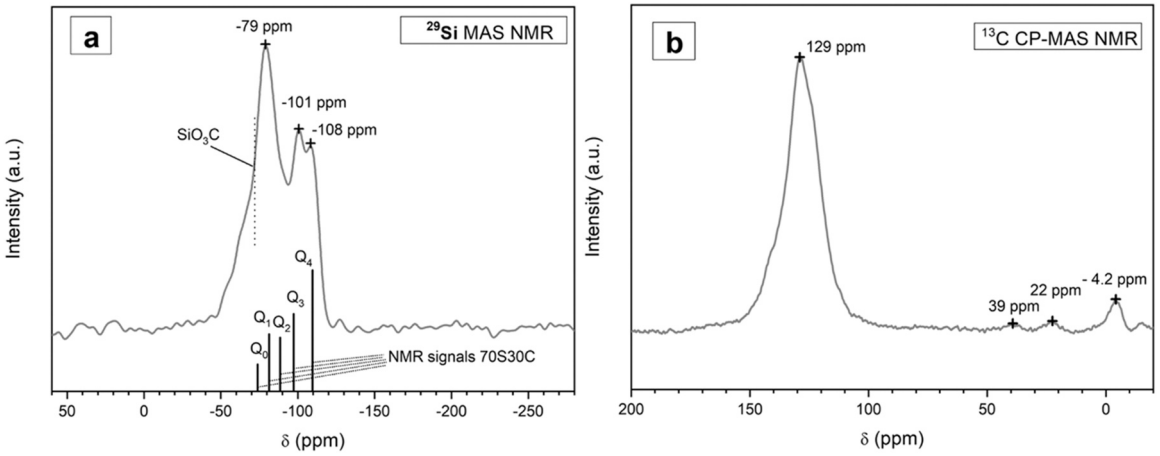

Fig. 5. NMR spectra of the obtained bioglass-C composite after firing at 700 °C; (a) ^{29}Si; (b)^{13}C.

dispersed phase; secondly, the printing layers were clearly distinguishable from each other.

A DSC-TG thermogram was collected to evidence the heat flows and the mass losses corresponding to the thermal evolution of printed scaffolds, as shown by Fig. 2. A complex series of events can be determined. From room temperature up to around 200 °C, events concerned Ca $(NO_3)_2{\cdot}4\ H_2O$ and silicone: in fact, the Ca salt first undergoes melting, at 40 °C [20], and then starts slowly to dehydrate from 130 up to 160 °C [21], giving origin to the first endo-thermic effect (Fig. 2a). The exo-thermic effect at about 200 °C is attributable to the cross-linking reaction of H44 [22]. Both dehydration of the Ca salt and cross-linking release water as by-product; the losses are even more visible from the differential mass loss plot (Fig. 2b).

Above 200 °C, a substantial heat release is attributed, up to 350 °C, to the decomposition of hardened acrylic resin [23]. Subsequent effects are due to the overlapping of contributions from the silicone and the calcium salt. The polymer-to-ceramic transformation of H44 is known to occur above 300 °C up to 550 °C [24]; $Ca(NO_3)_2$ is known to undergo decomposition into CaO (around 500 °C) [11] or melting (at 540 °C) [21]. The final ceramic yield (20 %, see Fig. 2b) is consistent with the hypothesis of complete burn-out of photocurable resin, decomposition of CaNT into CaO and transformation of H44 into a SiOC residue [4], as reported by Table 1.

The mixing between matrix and salt is further testified by the diffraction patterns in Fig. 3a. Diffraction peaks associated with Ca $(NO_3)_2{\cdot}4H_2O$ (PDF#26–1406) can be seen in the printed form. More interestingly, the firing at 700 °C, in nitrogen atmosphere, led to an X-ray amorphous material: the nitrate reasonably decomposed but not determined any CaO cluster; on the contrary, calcium ions remained dispersed in silicone-derived silica. The pattern of the fired material is actually very similar to that of 70S30C, obtained by firing silica gels modified by addition of the same Ca salt [25].

The fired material was actually a nanocomposite. Pyrolytic carbon is produced when silicones are converted to SiOC in nitrogen, developing an amorphous graphite-like nanocomposite distributed in a silica-rich glass matrix [1–3]; the separation of carbon motivates the black coloration in Fig. 1c,d. Higher magnification details (see Fig. 1d) reveal glassy, smooth surfaces, with no cracking.

The infrared spectroscopy (FTIR) analysis of the fired material, shown in Fig. 4a reveals bands (at 920 and 1030 cm^{-1}) consistent with mixed Si–O and Si–C bonds (Ren et al. [26] that observed the same shift from the standard [SiO_4] absorption, at 1080 cm^{-1}, to 1030 cm^{-1}). Si–C bonds were expected, considering the stoichiometry of H44-derived SiOC, as proposed by Scheffler et al. [27], consisting of $Si_3O_{4.6}C_{8.45}$. Such SiOC could be interpreted as a molecular mix of SiO_2, SiC and C in the following amounts:

$$Si_3O_{4.56}C_{1.92} \leftrightarrow 2.28\ SiO_2 + 0.72\ SiC + 1.2C$$

SiO_2 corresponds to about 76 wt% of the SiOC residue. This contribution, combined with the amount of fumed silica, was considered as the total silica amount. With the given proportions between constituents (see Table 1), the SiO_2/CaO balance resembled that of 70S30C bioglass (70 mol% SiO_2, 30 mol% CaO). As variously observed [28], the presence of fillers alters the ceramic yield of silicones, with destabilization of Si-C bonds; the low pyrolysis temperature, however, could favor the preservation. The Raman spectrum shown in Fig. 4b clearly exhibits peaks corresponding to graphite-like pyrolytic carbon, without any evidence from SiC nano-crystallites.

The Raman spectrum exhibits well-defined characteristic 'first-order' bands of graphite-like amorphous carbon, i.e. D band at 1350 cm^{-1} and G band at 1600 cm^{-1}, accompanied by 'second-order' bands at 2690 and 2930 cm^{-1}. The upshifting of G band and the marked asymmetry of D band might be attributed to the matrix surrounding pyrolytic carbon, in analogy with experiences on polymer-derived Biosilicate glass-ceramics [29]. The upshifting could be due to Si inclusion [30], whereas the 'shoulder' below 1200 cm^{-1} is consistent with contributions from amorphous silicate glass matrix. Raman studies of sol-gel derived glasses [31] have already evidenced signals from Si–O–Si bending vibrations at ~800 cm^{-1} (see the weak peak labelled as 'A'), from Si–O–NBO (non-bridging oxygen) at ~900 cm^{-1} (see the weak peak labelled as 'B') and from Si–O–Si stretching vibrations at 1100–1200 cm^{-1} (see the position labelled as 'C'). The weakness of the signals, in any case, do not support a clear identification. We cannot exclude, as an example, contributions from sp^3 carbon (known to yield a signal at 1170 cm^{-1} [32]).

Further structural information was collected by means of NMR spectroscopy. The ^{29}Si spectrum, shown in Fig. 5a, is interesting for the position of absorption peaks, expressed in terms of chemical shift (δ). Signals in the δ interval −70: −110 ppm are consistent with those of sol-gel derived 70S30C bioglass [33]. The relative intensity of the peaks, however, presents significant deviations: in sol-gel derived 70S30C (as shown by the histogram at the bottom of Fig. 5a) the dominant signal corresponds to Q_4 (SiO_4) units, at δ~−108 ppm, whereas in the newly developed material there is a strong peak at $\delta = -79$ ppm, with a quite large shoulder at δ~−50 ppm and δ~−60 ppm. The strong peak, in our opinion, cannot be explained as due to Q_0 (isolated SiO_2 tetrahedra) or Q_1 units; it could derive from the effective inclusion of carbon in the glass network, owing to Si–C bonds. Whereas no signal can be due to SiO_2C_2 or $SiOC_3$, we cannot exclude the presence of SiO_3C units, known to yield a signal at $\delta = -72$ ppm [34].

The ^{13}C spectrum confirms the presence of graphite-like carbon, with the strong signal at $\delta = 129$ ppm (typical of carbon in sp^2 hybridization); signals consistent with carbidic carbon (carbon in sp^3 hybridization,

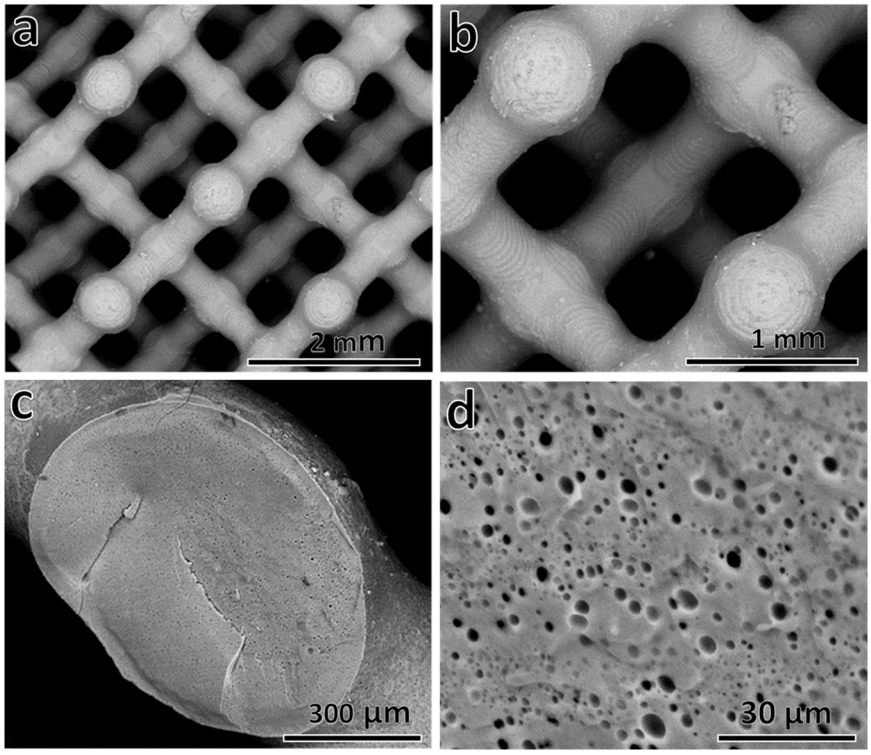

Fig. 6. Microstructural features of heat-treated scaffolds: (a) overview of diamond cell structure; (b) details of strut surface; (c) strut cross-section, (d) detail of internal porosity.

Table 2
Results from density and strength determinations.

Scaffold Design	Density values (g/cm^3)			Porosity [%]		Compressive Strength, σ_c (MPa)
	ρ_{geom}	ρ_{app}	ρ_{true}	Open	Total	
Diamond cell scaffold	0.38 ± 0.04	1.99 ± 0.02	2.2 ± 0.01	81 ± 2	83 ± 2	1.6 ± 0.2

typical of SiC, leading to peak at $\delta = 12$ ppm) were not detected [34]. The two resonances, at $\delta = 22$ ppm and $\delta = 39$ ppm, are attributable to residual aliphatic carbons [35]. The signal at −4.2 ppm is consistent with residual Si–CH_x bonds [36], which could come from the silicone resin.

Scanning electron microscopy analysis confirmed the homogeneity of the structure (Fig. 6a). Higher magnification details (Fig. 6b) reveal the absence of both cracks and chemical gradients (which would be evident, from the adopted backscattered electron imaging); interestingly, stair-step corrugations present in the as-printed struts (Fig. 1b) remained practically unaltered (Fig. 6b), as evidence of the absence of any viscous flow. Traces of gas evolution can be noticed only from pores in the strut cross-sections (Fig. 6c,d). Again, no chemical gradient (e.g. Ca or Si aggregates) can be observed according to the homogeneous colouration of the struts in the SEM image (Fig. 6c, resulting from the collection of backscattered electrons, in turn sensitive to the distribution of various elements). The uniformity concerns also the distribution of micrometric pores (Fig. 6d). The adopted, quite slow heat treatment evidently promoted a homogeneous gas release, with no local accumulation of gaseous by-products and pressure build-up. The large gas release (involving most constituents, from transformation of H44 to decomposition of acrylate residues and of Ca nitrate), resulted, besides in the microporosity of the struts, in a very significant shrinkage (nearly 40 % linear contraction).

Table 2 reports the results from density determinations. It can be observed that the open porosity (81 %) remained very close to the porosity of the adopted geometrical model (85 %). As shown by Fig. 6c and, more specifically, by Fig. 6d, the porosity was not completely open, with a multitude of closed pores, homogeneously distributed, visible from the cross-section. The value of true density, from pycnometry on crushed samples, is likely underestimated, since the same crushing could not lead to completely pore-free powders, in the presence of pores well below 5 µm (Fig. 6d). The underestimation is also supported by the literature, suggesting a true density of 70S30C bioglass in the order of 2.5 g/cm^3 [37].

The exact determination of true density is beyond the scope of the present investigation; the presence of many pores in the cross-section, on the contrary, is interesting in the analysis of the strength/density correlation. In fact, the observed compressive strength (σ_c=1.6 ± 0.2 MPa) is particularly high and could be associated to the particular chemistry of the glass matrix.

Considering the diamond lattice as a 'bending dominated' structure and neglecting the presence of closed porosity (i.e. considering the amount of open porosity as the total porosity), we could apply the well-recognized model for open-cell porous ceramics developed by Gibson and Ashby [38]. The model predicts the compressive strength (σ_c) of a brittle cellular body according to the relative density (ρ_{rel}, calculated as ρ_{rel}=1-P/100, considering P the total porosity) and the bending strength (σ_{bend}) of the solid material in the struts, as follows:

$$\sigma_c = C \cdot \sigma_{bend} \cdot \rho_{rel}^{3/2}$$

C is a dimensionless constant of approximately 0.2. With ρ_{rel}= 0.19 (81 % open porosity), the measured value of compressive strength is fitted by a σ_{bend} value exceeding 95 MPa, well above the bending strength of pore-free glass (for soda-lime glass the bending strength is ≈70 MPa [39]). In other words, the weakening caused by pores was likely counterbalanced by the strength enhancement provided by Si-C bonds (N and C bridges, in the structure of oxynitride and oxycarbide glasses, respectively, are known for their positive impact on mechanical properties [40,41]).

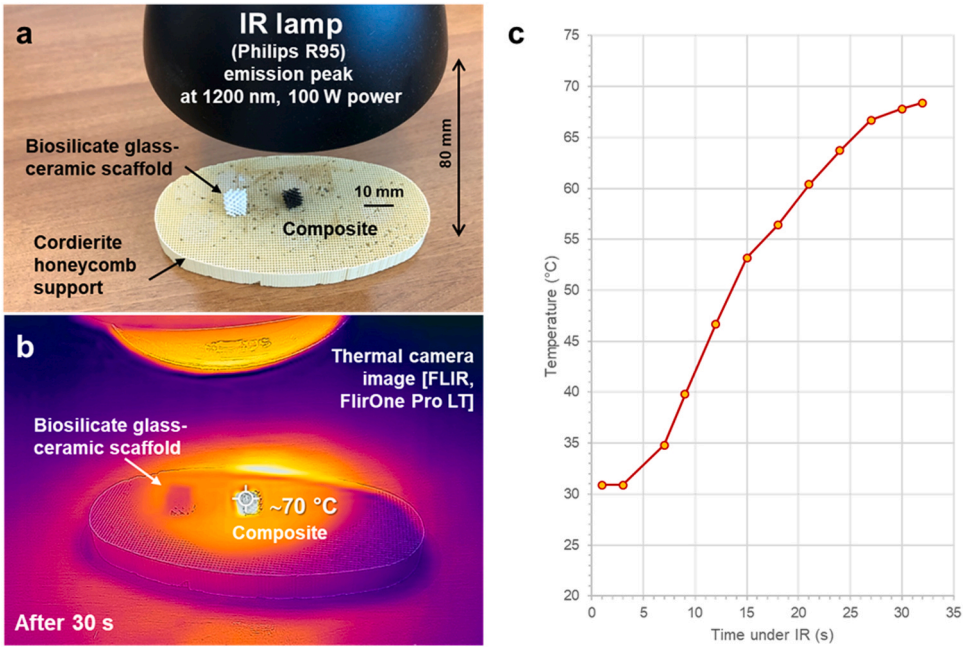

Fig. 7. (a) experimental setup for infrared heating test; (b) infrared camera picture after 30 s exposure; (c) heating curve.

The assessment of biocompatibility, bioactivity and bioresorbability of the newly developed scaffolds is in progress. A simple test, however, clearly illustrates the potential for photothermal effect, exploited in several carbon-containing bioceramic composites for both therapy and sterilization; in fact, carbon polymorphs act as powerful absorbers of infrared radiation [29]. Fig. 7a shows a composite scaffold under an IR lamp (commercial incandescent lamp Philips R95, with emission peak at $\lambda = 1200$ nm, 100 W; 80 mm distance) accompanied by a (C-free) Biosilicate® glass-ceramic scaffold [29]: only 30 s with IR lamp on suffice in determining the heating at nearly 70 °C (well above the threshold for disinfection from bacteria, ~55 °C [29]), as shown by the infrared camera picture in Fig. 7b. The rapid heating is further highlighted by the curve in Fig. 7c (data from a series of IR camera pictures). This means that the material would be easily sterilized using a higher power IR radiation source for a longer period of time or using an insulated chamber so as to reach a time-temperature combination in accordance to sterilization protocols [42].

4. Conclusions

A silicone-acrylate blend is confirmed to support vat photopolymerization 3D printing of oxycarbide ceramics. A fundamental finding of the present paper concerns the possibility to obtain a Ca-rich bioglass-based composite, by firing in nitrogen at 700 °C, of an engineered blend. Calcium nitrate tetrahydrate, previously known as calcium oxide precursor in sol-gel derived 70S30C bioglass, may be introduced in silicone-acrylate blends simply in nano-emulsion. The quasi-molecular distribution of the additive promotes both printing resolution and thermal transformation, with the definition of a glass matrix resembling 70S30C bioglass. Carbon from the pyrolysis of the silicone component is mainly involved in graphite-like dispersed phase (useful to enable the photothermal effect), but the inclusion also in the glass network cannot be excluded, according to FTIR and NRM spectroscopies.

CRediT authorship contribution statement

Franco M. Stabile: Conceptualization, Methodology, Validation, Formal analysis, Investigation, Data Curation, Writing; **Alessia Famengo:** Formal analysis, Investigation, Data Curation; **Danilo Pedron:** Formal analysis, Investigation, Data Curation; **Hamada Elsayed:** Conceptualization, Methodology, Validation, Formal analysis, Investigation, Data Curation, Writing, Writing - Review & Editing; **Enrico Bernardo:** Conceptualization, Methodology, Validation, Formal analysis, Resources, Data Curation, Writing - Review & Editing, Visualization, Supervision.

Declaration of Competing Interest

The authors declare no conflict of interest.

Data availability

The data that has been used is confidential.

Acknowledgements

The authors thank Ms Elena Tagliabue and Mr Marco Pettenuzzo (MSc students, University of Padova), for experimental assistance. FMS acknowledges the External Scholarship granted by the Scientific and Technical National Council (CONICET), Argentina.

References

[1] P. Colombo, G. Mera, R. Riedel, G.D. Sorarù, Polymer-derived ceramics: 40 years of research and innovation in advanced ceramics, J. Am. Ceram. Soc. 93 (2010) 1805–1837, https://doi.org/10.1111/j.1551-2916.2010.03876.x.
[2] E. Bernardo, L. Fiocco, G. Parcianello, E. Storti, P. Colombo, Advanced ceramics from preceramic polymers modified at the nano-scale: a review, Materials 7 (2014) 1927–1956, https://doi.org/10.3390/ma7031927.
[3] P. Colombo, E. Bernardo, G. Parcianello, Multifunctional advanced ceramics from preceramic polymers and nano-sized active fillers, J. Eur. Ceram. Soc. 33 (2013) 453–469, https://doi.org/10.1016/j.jeurceramsoc.2012.10.006.
[4] A. Dasan, H. Elsayed, J. Kraxner, D. Galusek, P. Colombo, E. Bernardo, Engineering of silicone-based mixtures for the digital light processing of Åkermanite scaffolds, J. Eur. Ceram. Soc. 40 (2020) 2566–2572, https://doi.org/10.1016/j.jeurceramsoc.2019.11.087.
[5] H. Elsayed, M. Picicco, A. Dasan, J. Kraxner, D. Galusek, E. Bernardo, Glass powders and reactive silicone binders: application to digital light processing of bioactive glass-ceramic scaffolds, Ceram. Int. 46 (2020) 25299–25305, https://doi.org/10.1016/j.ceramint.2020.06.323.

[6] J. Schmidt, P. Colombo, Digital light processing of ceramic components from polysiloxanes, J. Eur. Ceram. Soc. 38 (2018) 57–66, https://doi.org/10.1016/j.jeurceramsoc.2017.07.033.

[7] E. Zanchetta, M. Cattaldo, G. Franchin, M. Schwentenwein, J. Homa, G. Brusatin, P. Colombo, Stereolithography of SiOC ceramic microcomponents, Adv. Mater. 28 (2016) 370–376, https://doi.org/10.1002/adma.201503470.

[8] J. Schmidt, H. Elsayed, E. Bernardo, P. Colombo, Digital light processing of wollastonite-diopside glass-ceramic complex structures, J. Eur. Ceram. Soc. 38 (2018) 4580–4584, https://doi.org/10.1016/j.jeurceramsoc.2018.06.004.

[9] J.W. Halloran, V. Tomeckova, S. Gentry, S. Das, P. Cilino, D. Yuan, R. Guo, A. Rudraraju, P. Shao, T. Wu, T.R. Alabi, W. Baker, D. Legdzina, D. Wolski, W. R. Zimbeck, D. Long, Photopolymerization of powder suspensions for shaping ceramics, J. Eur. Ceram. Soc. 31 (2011) 2613–2619, https://doi.org/10.1016/j.jeurceramsoc.2010.12.003.

[10] G. Franchin, H. Elsayed, R. Botti, K. Huang, J. Schmidt, G. Giometti, A. Zanini, A. De Marzi, M. D'Agostini, P. Scanferla, Y. Feng, P. Colombo, Additive manufacturing of ceramics from liquid feedstocks, Chin. J. Mech. Eng. Add. Manuf. Front. 1 (2022), 100012, https://doi.org/10.1016/j.cjmeam.2022.100012.

[11] N. Travitzky, A. Bonet, B. Dermeik, T. Fey, I. Filbert-Demut, L. Schlier, T. Schlordt, P. Greil, Additive manufacturing of ceramic-based materials, Adv. Eng. Mater. 16 (2014) 729–754, https://doi.org/10.1002/adem.201400097.

[12] M. Porras, C. Solans, C. González, J.M. Gutiérrez, Properties of water-in-oil (W/O) nano-emulsions prepared by a low-energy emulsification method, Colloids Surf. A Physicochem. Eng. Asp. 324 (2008) 181–188, https://doi.org/10.1016/j.colsurfa.2008.04.012.

[13] R.K. Kesrevani, A. Sharma, Nanoarchitectured biomaterials: present status and future prospects in drug delivery, Nanoarch. Smart Del. Drug Target. (2016) 35–66, https://doi.org/10.1016/B978-0-323-47347-7.00002-1.

[14] A. Gupta, H.B. Eral, T.A. Hatton, P.S. Doyle, Nanoemulsions: formation, properties and applications, Soft Matter 12 (2016) 2826–2841, https://doi.org/10.1039/C5SM02958A.

[15] S. Zou, Y. Yang, H. Liu, C. Wang, Synergistic stabilization and tunable structures of Pickering high internal phase emulsions by nanoparticles and surfactants, Colloids Surf. A Physicochem. Eng. Asp. 436 (2013) 1–9, https://doi.org/10.1016/j.colsurfa.2013.06.013.

[16] M. Katsouli, S.A. Papatheodorou, V. Giannou, C. Tzia, Development of extra virgin olive and olive pomace oil nanoemulsions (o/w and w/o) enriched with surface-activephenolic compounds, J. Food Proc. Eng. 45 (2022), e13869, https://doi.org/10.1111/jfpe.13869.

[17] Z. Briceño-Ahumada, J.F.A. Soltero-Martínez, R. Castillo, Aqueous foams and emulsions stabilized by mixtures of silica nanoparticles and surfactants: a state-of-the-art review, Chem. Eng. J. Adv. 7 (2021), 100116, https://doi.org/10.1016/j.ceja.2021.100116.

[18] T.S. Horozov, B.P. Binks, T. Gottschalk-Gaudig, Effect of electrolyte in silicone oil in-water emulsions stabilised by fumed silica particles, Phys. Chem. Chem. Phys. 9 (2007) 6398–6404, https://doi.org/10.1039/B709807N.

[19] G. Sádovská, P. Honcová, R. Pilař, L. Oravová, D. Honc, Calorimetric study of calcium nitrate tetrahydrate and magnesium nitrate hexahydrate, J. Therm. Anal. Calorim. 124 (2016) 539–546, https://doi.org/10.1007/s10973-015-5159-y.

[20] W.M. Haynes, D.R. Lide, T.J. Bruno, CRC handbook of chemistry and physics, CRC Press, 2016, https://doi.org/10.1201/9781315380476.

[21] A. Migdał-Mikuli, J. Hetmańczyk, Ł. Hetmańczyk, Thermal behaviour of $[Ca(H_2O)_4](NO_3)_2$, J. Therm. Anal. Calorim. 89 (2007) 499–503, https://doi.org/10.1007/s10973-006-7526-1.

[22] A. Tolosa, B. Krüner, N. Jäckel, M. Aslan, C. Vakifahmetoglu, V. Presser, Electrospinning and electrospraying of silicon oxycarbide-derived nanoporous carbon for supercapacitor electrodes, J. Power Sources 313 (2016) 178–188, https://doi.org/10.1016/j.jpowsour.2016.02.077.

[23] Y. Feng, X. Guo, K. Huang, H. Elsayed, G. Franchin, H. Gong, P. Colombo, Enhanced electromagnetic microwave absorption of SiOC ceramics targeting the integration of structure and function, J. Eur. Ceram. Soc. 41 (2021) 6393–6405, https://doi.org/10.1016/j.jeurceramsoc.2021.06.007.

[24] S. Bhattacharjee, P. Ranjan Das, C. Ohl, V. Wilker, M. Kappa, F. Scheffler, M. Scheffler, Novel-type inorganic foams from preceramic polymers with embedded titania nanoparticles for photo-catalytic applications, Adv. Eng. Mater. 13 (2011) 996–1001, https://doi.org/10.1002/adem.201100025.

[25] E. Norris, C. Ramos-Rivera, G. Poologasundarampillai, J.P. Clark, Q. Ju, A. Obata, J.V. Hanna, T. Kasuga, C.A. Mitchell, G. Jell, J.R. Jones, Electrospinning 3D bioactive glasses for wound healing, Biomed. Mater. 15 (2020), 015014, https://doi.org/10.1088/1748-605X/ab591d.

[26] Z. Ren, W. Zhou, Y. Qing, S. Duan, H. Pan, X. Chai, Y. Zhou, Simultaneously improving mechanical and microwave absorption properties of a novel SiC_f/SiOC & mullite hybrid ceramic matrix composite, J. Eur. Ceram. Soc. 41 (2021) 7560–7571, https://doi.org/10.1016/j.jeurceramsoc.2021.07.065.

[27] M. Scheffler, T. Takahashi, J. Kaschta, H. Muensted, P. Buhler, P. Greil, Pyrolytic decomposition of preceramic organo polysiloxanes, Innovative Processing and Synthesis of Ceramics, Glasses, and Composites IV: Ceramic Trans (USA) 115 (2000) 239–250.

[28] L. Fiocco, S. Agnoli, D. Pedron, M. Secco, S. Tamburini, L. Ferroni, C. Gardin, B. Zavan, E. Bernardo, Wollastonite-diopside-carbon composite foams from a silicone resin and inorganic fillers, Ceram. Int. 44 (2018) 931–937, https://doi.org/10.1016/j.ceramint.2017.10.025.

[29] F. Dogrul, S. Bortolin, D. Del Col, N. Dengo, D. Pedron, M. Michalek, H. Elsayed, D. Galusek, E. Bernardo, Polymer-derived Biosilicate-C composite foams: phase development and photothermal effect, J. Eur. Ceram. Soc. 41 (2021) 380–388, https://doi.org/10.1016/j.jeurceramsoc.2021.09.012.

[30] Z. Wang, P. Li, Y. Chen, J. Liu, W. Zhang, Z. Guo, M. Dong, Y. Li, Synthesis, characterization and electrical properties of silicon-doped graphene films, J. Mater. Chem. C. 3 (2015) 6301–6306, https://doi.org/10.1039/C5TC00563A.

[31] H. Aguiar, J. Serra, P. González, B. León, Structural study of sol–gel silicate glasses by IR and Raman spectroscopies, J. Non-Cryst. Sol. 355 (2009) 475–480, https://doi.org/10.1016/j.jnoncrysol.2009.01.010.

[32] H. Yoshinaka, S. Inubushi, T. Wakita, T. Yokoya, Y. Muraoka, Formation of Q-carbon by adjusting sp^3 content in diamond-like carbon films and laser energy density of pulsed laser annealing, Carbon 167 (2020) 504–511, https://doi.org/10.1016/j.carbon.2020.06.025.

[33] S. Lin, C. Ionescu, K.J. Pike, M.E. Smith, J.R. Jones, Nanostructure evolution and calcium distribution in sol–gel derived bioactive glass, J. Mater. Chem. 19 (2009) 1276–1282, https://doi.org/10.1039/B814292K.

[34] S.J. Widgeon, S. Sen, G. Mera, E. Ionescu, R. Riedel, A. Navrotsky, ^{29}Si and ^{13}C Solid-state NMR spectroscopic study of nanometer-scale structure and mass fractal characteristics of amorphous polymer derived silicon oxycarbide ceramics, Chem. Mater. 22 (2010) 6221–6228, https://doi.org/10.1021/cm1021432.

[35] P. Liu, Y. Zhang, T. Pan, D. Zhang, L. Chen, C. Sun, Accurately quantifying carbon structural types and predicting pyrolysis behavior of coal using solid 13C NMR Cp/MAS spectra, Fuel 327 (2022), 125092, https://doi.org/10.1016/j.fuel.2022.125092.

[36] Z. Ren, C. Gervais, G. Singh, Fabrication and characterization of silicon oxycarbide fibre-mats via electrospinning for high temperature applications, RSC Adv. 10 (2020) 38446–38455, https://doi.org/10.1039/D0RA04060F.

[37] S. Midha, T.B. Kim, W. Bergh, P.D. Lee, J.R. Jones, C.A. Mitchell, Preconditioned 70S30C bioactive glass foams promote osteogenesis in vivo, Acta Biomater. 9 (2013) 9169–9182, https://doi.org/10.1016/j.actbio.2013.07.014.

[38] L.J. Gibson, M.F. Ashby, Cellular Solids: Structure and Properties, Cambridge University Press, Cambridge, UK, 1997, https://doi.org/10.1017/CBO9781139878326.

[39] J.J. Mecholsky, R.W. Rich, S.W. Freiman, Prediction of fracture energy and flaw size in glasses from measurements of mirror size, J. Am. Ceram. Soc. 57 (1974) 440–443, https://doi.org/10.1111/j.1151-2916.1974.tb11377.x.

[40] S. Hampshire, Oxynitride glasses, J. Eur. Ceram. Soc. 28 (2008) 1475–1483, https://doi.org/10.1016/j.jeurceramsoc.2007.12.021.

[41] C. Moysan, R. Riedel, R. Harshe, T. Rouxel, F. Augereau, Mechanical characterization of a polysiloxane-derived SiOC glass, J. Eur. Ceram. Soc. 27 (2017) 397–403, https://doi.org/10.1016/j.jeurceramsoc.2006.01.016.

[42] W.A. Rutala, D.J. Weber, and the Healthcare Infection Control Practices Advisory Committee (HICPAC), Guideline for Disinfection and Sterilization in Healthcare Facilities (2008), https://stacks.cdc.gov/view/cdc/47378/cdc_47378_DS1.pdf.